Transient Power Angle Stability Analysis of Grid-Forming Converters Under Resistive Short-Circuit Faults

Xiaoyang Deng[1,*], Xiaoliang Zhu[2], Yan Hu[2], Desheng Wang[1], Xiao Wang[1], Tianyu Su[1], Xiangwu Yan[2]

[1]State Grid Jibei Electric Co., Ltd. Research Institution (North China Electric Power Research Institution Co., Ltd.), Beijing, China
[2]Hebei Key Laboratory of Distributed Energy Storage and Micro-grid (North China Electric Power University), Hebei, China

Corresponding author: Xiaoyang Deng (e-mail: dengxiaoyang126@126.com).

ABSTRACT This paper examines the transient power-angle stability of grid-forming converters (GFMs) subjected to grid faults. Existing studies commonly simplify the network as a purely inductive line and use ideal fault assumptions, which makes it difficult to describe how practical fault conditions influence power transmission and stability. A fault analytical model that includes line resistance is therefore constructed, and a closed-form Pe-delta relationship is obtained with offset, amplitude, and phase-shift components. Fault position, transition resistance, the line impedance ratio, and short-circuit ratio are incorporated into the model. On the basis of the equal-area criterion, the transient instability process of GFMs under different fault types is analyzed. MATLAB/Simulink results verify both the proposed expression and the corresponding stability mechanism. A further scan of the transient stability region shows that resistance-grounded and reactance-grounded faults present different stability distributions when the grid and fault parameters vary.

INDEX TERMS Grid-Forming Converter; Power-Angle Transient Stability; Fault Parameter Diversity; Analytical Modeling

I. INTRODUCTION

As new-type power systems develop, the share of renewable generation and power-electronic equipment in conventional grids continues to rise [1]. This trend weakens system inertia and makes weak-grid behavior more evident [2,3]. Grid-forming converters can establish voltage and frequency without relying completely on an external reference [4], and thus offer an important means of supporting weak grids and improving the integration stability of renewable energy [5]. During either asymmetrical [6] or symmetrical grounding faults, however, GFMs may experience a large excursion of the power angle, loss of synchronization strength, or disconnection from the grid [7]. For this reason, transient stability analysis of GFMs under complicated fault conditions is essential for secure converter and power-system operation. Research on GFM transient stability has produced many useful results [8,9]. The equal-area criterion, first used in conventional power-system studies, was applied to GFM stability problems in [10] and [11], where power-angle motion under simplified voltage-sag conditions was obtained. Later studies introduced damping into the analysis [12,13], making it possible to evaluate how damping coefficients change the transient stability margin.

In addition, [14] quantitatively studied transient synchronization stability in virtual synchronous generators and clarified how virtual inertia interacts with damping. Nevertheless, the assumptions adopted in many available models are still too ideal for practical fault assessment. For example, [10] places the fault directly at the point of common coupling, so the change in equivalent network impedance caused by fault distance is ignored. In [15], the line is treated as purely inductive, and neither transition resistance nor the impedance ratio is considered. Although weak-grid operation is discussed in [16], fault distance and transition resistance are absent from the analytical model. The work in [17] considers only the short-circuit ratio, while [18] includes both SCR and X/R but does not combine them with fault position and transition resistance in one unified formulation. Consequently, an analytical framework that can simultaneously describe several fault-related parameters under complex conditions is still needed. Without such a framework, the stability of GFMs in very weak grids, remote fault cases, and high-resistance grounding scenarios may be inaccurately assessed, and the predicted stability margin may be more optimistic than the actual dynamic response.

When a complex fault occurs, the fault location, SCR, and X/R may change at the same time, thereby reshaping the power-transfer relation between the converter and the grid. A model based only on terminal faults and purely inductive lines cannot fully reproduce this transient power-angle behavior. Accordingly, this paper establishes an integrated analytical method that considers fault position, transition resistance,

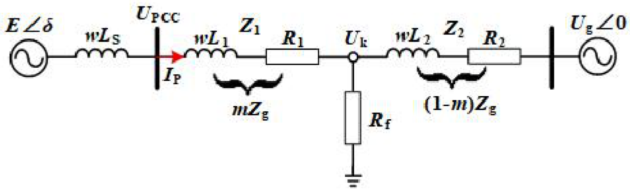

FIGURE 1. Equivalent Circuit Used for the GFM under Fault Conditions

frequency-related X/R, and SCR. The X/R term is especially relevant in low-frequency systems, because the influence of line resistance becomes more prominent [19]. Simulation results are used to verify the proposed method.

II. FAULT POWER-ANGLE CHARACTERISTICS OF GFM

A. ANALYTICAL MODELING OF POWER UNDER FAULT CONDITIONS

To study how line resistance affects fault power-angle behavior, the equivalent network shown in Figure. 1 is used. In low-frequency generating-unit systems, the resistive part of the transmission line cannot be ignored. In addition, when a bolted short-circuit fault is considered, the grounding path is more appropriately represented by a transition resistance than by a transition reactance. In the equivalent circuit, the GFM is modeled as a controlled internal voltage source E∠δ connected to the grid through the filter reactance Xs. The grid-side equivalent voltage is Ug∠0. The complete line impedance is written as Zg=R_g+jX_g, where R_g and X_g are the equivalent resistance and reactance of the line. If the fault point is located at the fraction m measured from the point of common coupling, the impedances on the two sides of the fault are Z1=mZg and Z2=(1-m)Zg, respectively, and the grounding transition resistance is R_f.

Using the current balance at the fault node together with the loop-voltage equations, the grid-connected current during the fault can be obtained analytically. To keep the main text concise, the detailed derivation is placed in Appendix A. The complex power at the internal voltage terminal is given by

$$S = P + jQ = Ee^{j\delta} I_p^* \tag{1}$$

power measured at the GFM internal voltage terminal. Thus, their changes include not only the transmission of power to the grid, but also the dissipation introduced by the line resistance and the fault branch. The active and reactive powers under fault conditions can therefore be written as

$$\begin{cases} P = E^2 \dfrac{[R_f + (1-m)R_g]D_R + (1-m)X_g D_I}{|D|^2} \\ \qquad - \dfrac{R_f E U_g}{|D|} \cos(\delta + \gamma), \\ Q = E^2 \dfrac{[R_f + (1-m)R_g]D_I - (1-m)X_g D_R}{|D|^2} \\ \qquad - \dfrac{R_f E U_g}{|D|} \sin(\delta + \gamma) \end{cases} \tag{2}$$

where these coefficients are functions of the equivalent impedance, the fault-position coefficient, and the transition resistance.

$$\begin{aligned} &D = D_R + jD_I, \qquad \gamma = \arctan(D_I/D_R), \\ &D_R = R_f R_g + m(1-m)(R_g^2 - X_g^2) - (1-m)X_s X_g, \\ &D_I = R_f(X_s + X_g) + R_g[(1-m)X_s + 2m(1-m)X_g] \end{aligned} \tag{3}$$

For subsequent discussion, (2) is rearranged into the following form

$$\begin{aligned} P(\delta) &= P_0 - A\cos[\delta + \gamma], \\ Q(\delta) &= Q_0 - A\sin[\delta + \gamma] \end{aligned} \tag{4}$$

Equation (4) shows that, once line resistance is included, the active and reactive powers in the fault interval can be represented by trigonometric expressions containing an offset component (P_0, Q_0), an amplitude component (A), and a phase-shift component (γ). These components depend on R_g, m, R_f, and X_g. Therefore, unlike the purely inductive-line model, the resistance-inclusive model changes the mathematical form of the fault power curve. The expressions above provide the basis for evaluating the influence of different parameters on the power-angle characteristics.

B. THE EFFECTS OF SYSTEM PARAMETERS ON FAULT POWER-ANGLE CHARACTERISTICS

Using the model derived in Section 2.1, this section examines how fault-network parameters modify the power-angle curves. The base values are E=1.05∠δ, Ug=1∠0, Xs=0.15, R_f=0.04, SCR=2, X/R=7, and m=0.5. Starting from this operating point, the fault-position coefficient m, transition resistance R_f, line impedance ratio X/R, and short-circuit ratio are adjusted separately, and the resulting active-and reactive-power variations with the power angle are analyzed.

1) EFFECT OF FAULT LOCATION ON POWER-ANGLE CHARACTERISTICS

Keeping the other parameters unchanged, m is selected as 0.2, 0.5, and 0.8 to compare the power-angle curves for different fault positions. According to (4), P_0, Q_0, A, and γ correspond to the offset, amplitude, and phase-shift terms. The coefficient m changes the curves in two ways. First, it directly modifies the offsets of the active-and reactive-power curves through

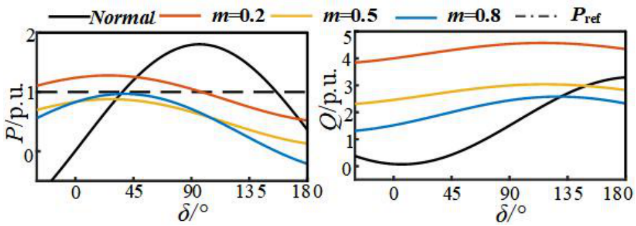

FIGURE 2. Power-Angle Curves Corresponding to Different Fault-Position Coefficients m

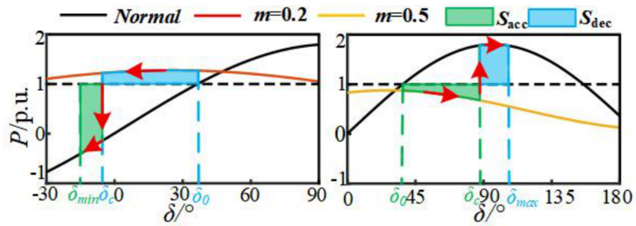

FIGURE 3. Acceleration and Deceleration Areas under Different Fault-Position Coefficients m

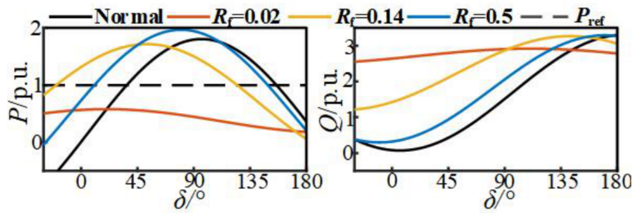

FIGURE 4. Power-Angle Curves under Different Fault Transition Resistances R_f

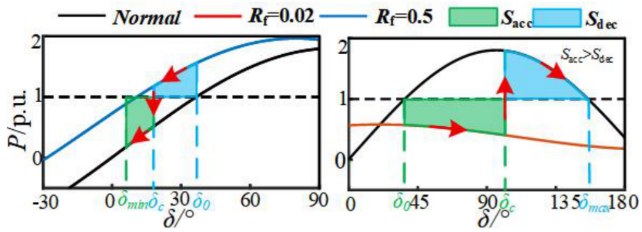

FIGURE 5. Acceleration and Deceleration Areas under Different Transition Resistances R_f

(1-m)R_g and (1-m)X_g. Second, it changes |D| and γ through Dr and Di, which further adjusts the amplitude and phase distribution.

Figure. 2 shows that $P_e(Q_e)$–δ varies clearly as m changes. When m becomes larger, the offset, amplitude, and phase-shift terms are altered, so the P_e–δ curve moves downward and its maximum value decreases. This means that the source-side active-power delivery capability is reduced. The Q_e–δ curve also moves downward as m increases, indicating that fault position changes both the active-power and reactive-power angle characteristics. Hence, the coefficient m has an important influence on the power-angle curve and on the transient stability margin.

The acceleration and deceleration areas for different values of m are further displayed in Figure. 3. During the fault, the movement of the power angle mainly depends on the relative position of the fault active-power curve and P_{ref}. If Pe is below P_{ref}, δ is accelerated and increases; if Pe is above P_{ref}, δ tends to decelerate and decrease. For m=0.2, the value of Pe corresponding to the post-fault power angle is higher than P_{ref}, so a reverse deceleration tendency appears and the transient stability is improved. For m=0.5 and m=0.8, Pe is lower than P_{ref}, which enlarges the acceleration tendency of δ and reduces the stability margin.

2) EFFECT OF FAULT TRANSITION RESISTANCE ON POWER-ANGLE CHARACTERISTICS

To analyze the role of transition resistance, R_f is assigned values of 0.02, 0.14, and 0.5 p.u. As can be seen from (4), R_f changes not only P_0, Q_0, and A, but also |D| and γ through Dr and Di. Thus, changing R_f simultaneously adjusts the offset, the amplitude, and the phase distribution of the fault power-angle curves.

As Figure. 4 illustrates, increasing R_f pushes the P_e–δ curve upward and makes it approach the normal operating curve. A larger R_f reduces the current-shunting effect of the fault branch, so the active-power transfer capacity of the system is improved. At the same time, the Q_e–δ curves for different R_f values intersect with one another, which indicates that transition resistance also changes the reactive-power angle characteristics by acting on the offset, amplitude, and phase terms.

Figure. 5 gives the acceleration-deceleration-area distribution under different R_f values. When R_f=0.02, the fault curve near the initial operating point lies far below P_{ref}, so δ is accelerated and the acceleration area dominates. If the deceleration area available after fault clearing cannot compensate for the accumulated kinetic energy, instability may occur. By contrast, when R_f=0.5, the fault curve is close to, or even higher than, P_{ref} in the corresponding interval, and δ tends to decelerate. These observations show that a higher R_f decreases the acceleration area, increases the deceleration area, and improves the transient stability margin.

3) EFFECTS OF FREQUENCY-DEPENDENT LINE IMPEDANCE CHARACTERISTICS ON FAULT POWER-ANGLE CHARACTERISTICS

The base parameters are then retained while X/R is set to 2, 7, and 15. These three cases represent different frequency-related line impedance characteristics and are used to evaluate the effect of X/R on the power-angle response. For a fixed SCR, changing X/R changes the proportions of R_g and X_g, and therefore affects P_0, Q_0, A, |D|, and γ.

As presented in Figure. 6, an increase in X/R means that X_g accounts for a larger share of the line impedance while R_g becomes smaller. Under this condition, active-power support is weakened. The P_e–δ curves for all studied cases therefore shift downward, and their main peak values decrease gradually. In contrast, the reactive-power support capability

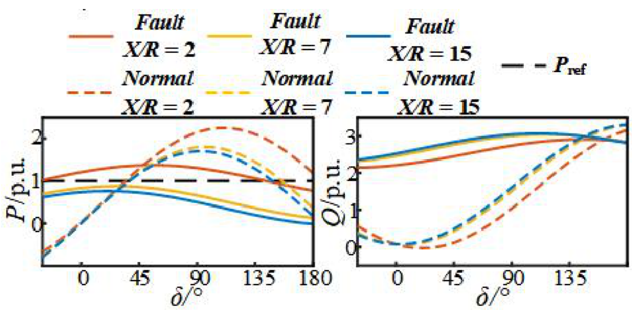

FIGURE 6. Power-Angle Curves for Different Line Impedance Ratios X/R

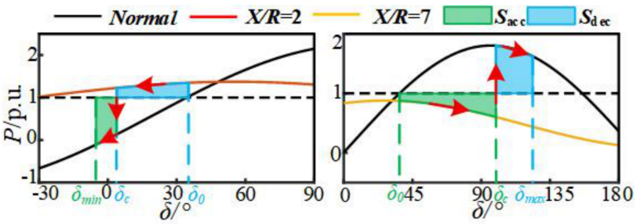

FIGURE 7. Acceleration and Deceleration Areas for Different X/R Values

increases with X/R, and the Q_e–δ curves move upward as a whole.

Figure. 7 compares the acceleration and deceleration areas for different impedance ratios. The case X/R=2 corresponds to a low-frequency condition in which the reactance share is smaller and the resistive feature is more obvious. At the fault instant, the P_e–δ curve is higher than P_{ref}, so the deceleration area is dominant. As frequency rises, the equivalent line reactance X_g=ωLg increases and X/R becomes larger. When X/R≥7, the fault P-δ curve lies further below P_{ref}, which causes the acceleration area to dominate and weakens the transient stability margin.

4) EFFECT OF SHORT-CIRCUIT RATIO ON FAULT POWER-ANGLE CHARACTERISTICS

With the reference parameters unchanged, SCR is selected as 1.2, 2, and 5 to evaluate the effect of grid strength on the fault power-angle behavior. In this part, X/R is fixed; therefore, changing SCR is equivalent to changing the magnitude of the grid-side impedance |Zg| in per-unit form, namely

$$|Z_g| = \frac{1}{\text{SCR}} \tag{5}$$

According to (4), SCR changes R_g and X_g at the same time. As a result, the offset, amplitude, and phase-shift terms are modified, and the overall power-angle distribution is reshaped.

Figure. 8 demonstrates that the P_e–δ curves differ considerably among SCR cases. A higher SCR represents stronger coupling between the converter and the grid, which improves active-power support. Therefore, the P_e–δ curves move upward for all operating conditions. Meanwhile, the reduction in X_g associated with a higher SCR strengthens the reactive-power exchange ability, so the Q_e–δ curves also shift upward.

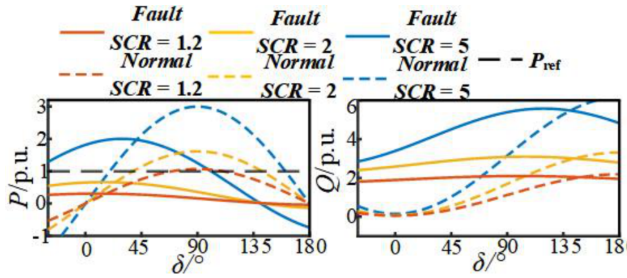

FIGURE 8. Power-Angle Curves Obtained for Different Short-Circuit Ratios SCR

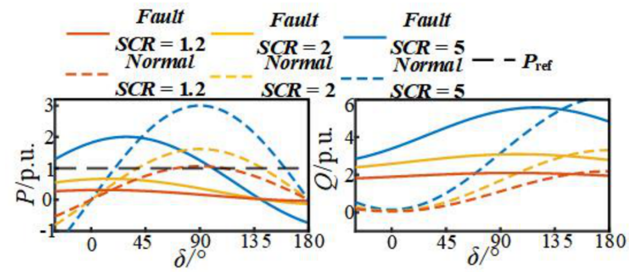

FIGURE 9. Acceleration and Deceleration Areas under Different Short-Circuit Ratios SCR

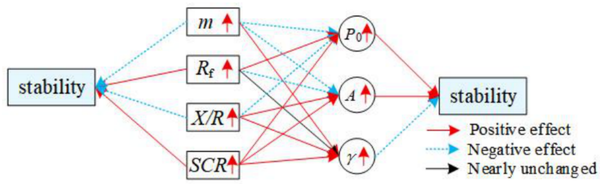

FIGURE 10. Parameter Influence Paths for Transient Stability

The area distribution for different SCR values is shown in Figure. 9. At SCR=1.2, the acceleration area is dominant during the fault, while the deceleration area after fault clearing is not large enough, leading to a smaller stability margin and a greater possibility of losing synchronism. When SCR increases to 5, the deceleration area dominates at the early fault stage, allowing the system to move back toward the stable operating point after the power-angle curve is restored.

C. QUALITATIVE ANALYSIS OF THE EFFECTS OF DIFFERENT SYSTEM PARAMETERS

From (4), the fault power-angle curve is governed together by the offset term P_0, amplitude term A, and phase term γ. As summarized in Figure. 10, system parameters affect transient stability by changing one or more of these three terms.

A larger P_0 lifts the fault P_e–δ curve and narrows the acceleration area, whereas a larger A increases the curve peak and broadens the post-fault deceleration area. Both changes generally improve stability. In contrast, a larger γ moves the curve to the left, lowers δmax=180°−γ, and reduces the available deceleration region. More specifically, increasing m decreases P_0 and A and usually raises γ, so the stability margin is reduced. Increasing R_f mainly raises P_0 and is beneficial.

A higher frequency raises X/R; although A may increase, the decrease of P_0 and the increase of γ become dominant and stability deteriorates. Increasing SCR raises both P_0 and A, and its stabilizing effects outweigh the moderate increase in γ.

III. SIMULATION VALIDATION UNDER DIFFERENT SYSTEM PARAMETERS

A MATLAB/Simulink model is built to verify the analytical model. The time-domain responses and P_e–δ trajectories are examined under variations in fault position, transition resistance, frequency-related X/R, and SCR.

A. TIME-DOMAIN SIMULATION VALIDATION UNDER DIFFERENT SYSTEM PARAMETERS

Figure. 11 shows the time-domain responses for different parameter settings. The fault location m changes the fault-period power-transfer relationship and therefore affects power, power angle, and current responses. A smaller R_f produces a deeper PCC voltage sag and stronger oscillation, whereas increasing R_f improves the dynamic recovery. When system frequency increases, the equivalent line reactance and X/R increase, which weakens active-power support, enlarges oscillations, and slows the post-fault recovery process. By comparison, a larger SCR enhances both power-transfer and voltage-support capability and helps the system recover after the fault.

In general, the time-domain results verify that fault position, transition resistance, frequency-dependent X/R, and SCR all influence the post-fault power-angle dynamics. Larger R_f and SCR improve transient stability, while a higher X/R reduces active-power support and decreases the stability margin. These simulation observations agree with the preceding power-angle-curve and area analyses, confirming the validity of the analytical model.

B. PE-Δ TRAJECTORIES UNDER DIFFERENT SYSTEM PARAMETERS

To further show how the parameters affect power transmission and power-angle motion during a fault, the simulated P_e–δ trajectories are plotted in Figure. 12. The arrows mark the trajectory direction, and δ_0 represents the power angle at the pre-fault steady state.

As indicated in Figure. 12, the fault location m changes the size of trajectory deviation and the recovery route, although all three cases return near the stable operating point after fault clearing. Increasing R_f reduces the power-angle excursion and improves the recovery process, whereas R_f=0.02 causes the trajectory to diverge and the system to become unstable. Increasing frequency and X/R enlarges the oscillation range and lengthens the recovery path, reducing the transient stability margin. A higher SCR suppresses trajectory deviation and oscillation and speeds up post-fault recovery. These results are consistent with the theoretical P_e–δ characteristics.

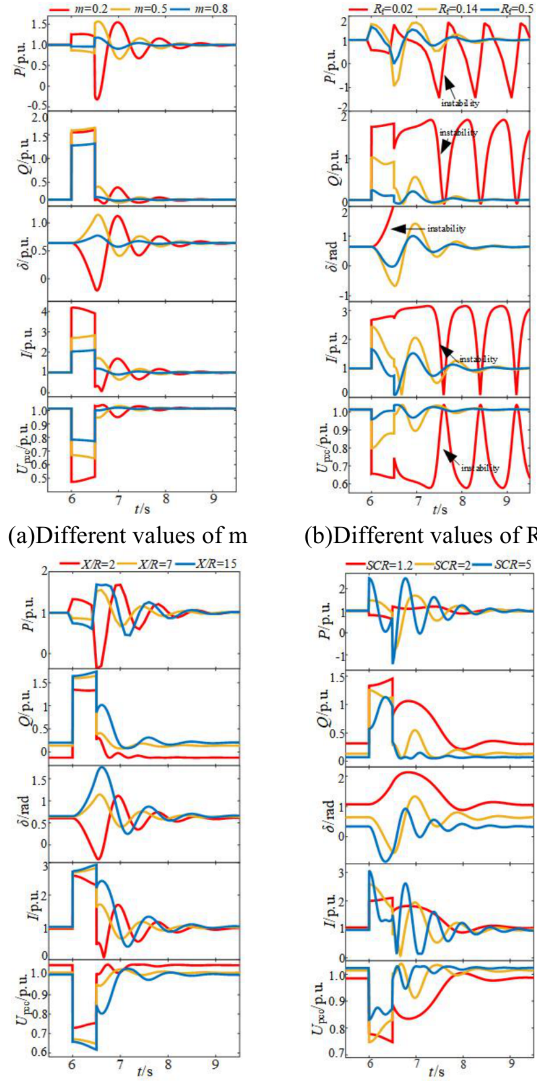

(a)Different values of m (b)Different values of R_f

(c) Different values of X/R (d) Different values of SCR

FIGURE 11. Time-Domain Responses under Fault Conditions for Different System Parameters

IV. SIMULATION VALIDATION OF TRANSIENT STABILITY REGIONS UNDER DIFFERENT SYSTEM PARAMETERS

For a further check of the proposed model, fault depth and fault duration are scanned under different system parameters, and resistance-grounded faults are compared with reactance-grounded faults. The converter is regarded as stable when its power angle remains below π during and after the fault. The corresponding transient stability regions are then evaluated quantitatively.

A. SIMULATION VALIDATION OF TRANSIENT STABILITY REGIONS UNDER RESISTANCE-GROUNDED FAULTS WITH DIFFERENT GRID PARAMETERS

The transient stability regions obtained by varying m, frequency-related X/R, and SCR are shown in Figure. 13.

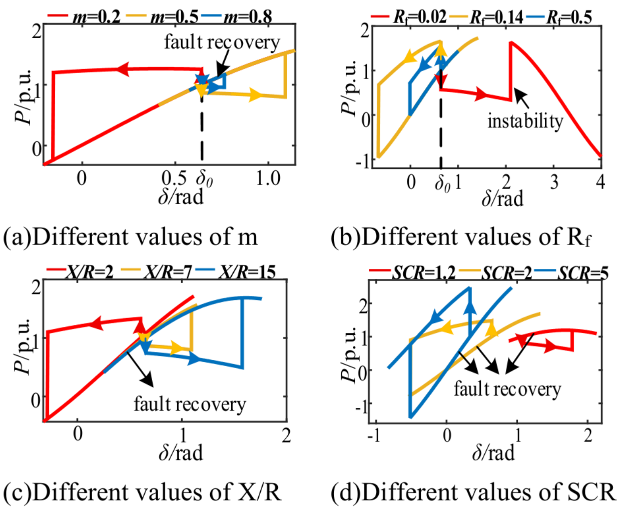

FIGURE 12. Simulated P_e−δ Trajectories for Different Parameters under Fault Conditions

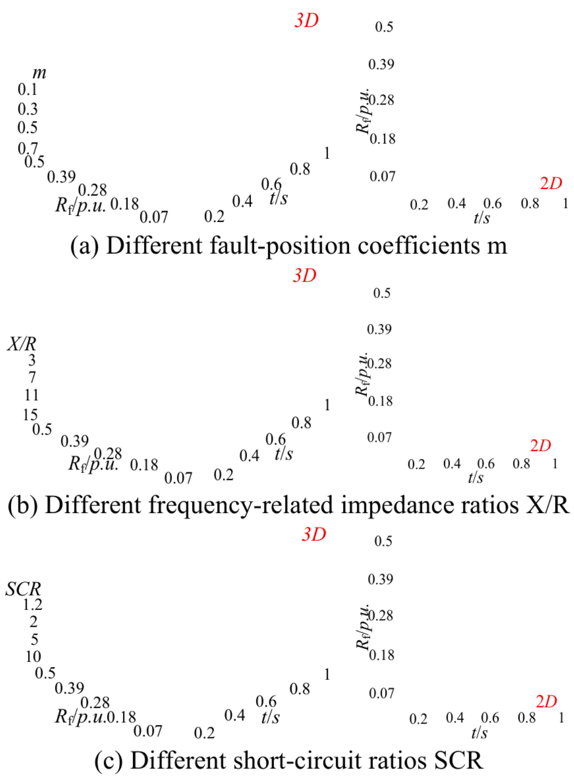

FIGURE 13. Transient Stability Regions under Different Faulted-Grid Parameters

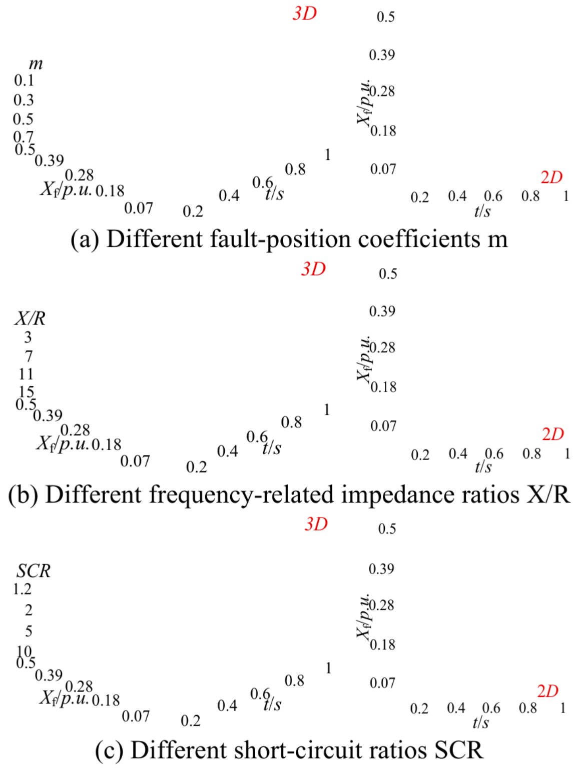

FIGURE 14. Transient Stability Regions for Reactance-Grounded Faults with Different Grid Parameters

Colored solid markers represent stable operating points, and the right-side panels provide two-dimensional top views of the same results. Different colors are used to identify the cases associated with different values of m, X/R, and SCR.

nonmonotonic manner with the fault location m, and the largest number appears at an intermediate location. This means that the stability margin is greatest in that case. As the system frequency rises, the equivalent line reactance and X/R increase, and fewer stable points are obtained. In addition, the stable-point number increases with SCR, demonstrating that stronger grid conditions enlarge the transient stability region.

B. SIMULATION VALIDATION OF TRANSIENT STABILITY REGIONS UNDER REACTANCE-GROUNDED FAULTS WITH DIFFERENT GRID PARAMETERS

Next, the transition resistance R_f is replaced by the transition reactance X_f, and simulations are repeated under the same parameter settings. Figure. 14 presents the quantitative transient-stability-region results for reactance-grounded faults. The stable-point numbers are listed in Table II and are compared with the corresponding resistance-grounded cases.

As listed in Table II, the parameter influences on the transient stability regions are similar to those obtained for resistance-grounded faults. The stable-point number still changes nonmonotonically with m; increasing X/R is unfavorable to stability; and increasing SCR improves the stability region. However, for all parameter cases, the total number of stable points under reactance-grounded faults is smaller than that under resistance-grounded faults. This result indicates that an inductive transition impedance is more adverse to transient stability than a resistive transition impedance, particularly when SCR is low.

TABLE 1. Stable-Point Numbers in the Transient Stability Regions for Different Faulted-Grid Parameters

Parameter	Case 1	Case 2	Case 3	Case 4	Total	Percentage (%)
m	0.1: 90	0.3: 96	0.5: 94	0.7: 94	374	93.5
X/R	3: 100	7: 96	15: 94	30: 94	384	96
SCR	1.2: 83	2: 94	5: 100	10: 100	377	94.25

TABLE 2. Stable-Point Numbers in the Transient Stability Regions for Different Reactance-Grounded Faulted-Grid Parameters

Parameter	Case 1	Case 2	Case 3	Case 4	Total	Percentage (%)
m	0.1: 84	0.3: 85	0.5: 85	0.7: 82	336	84
X/R	3: 95	7: 85	15: 75	30: 76	331	82.75
SCR	1.2: 53	2: 85	5: 93	10: 91	322	80.5

V. CONCLUSIONS

This paper develops an analytical fault power-angle model that incorporates both line resistance and transition resistance, and the effects of several important parameters are verified through simulations. After line resistance is included, the fault power-angle curves show coupled changes in offset, amplitude, and phase. Fault location, transition resistance, line impedance ratio, and short-circuit ratio alter the fault-period power balance by changing these terms, thereby influencing the power-angle trajectory and transient stability. Increasing R_f raises the offset term and enhances stability; higher frequency increases X/R and strengthens the phase shift, which usually reduces stability; and increasing SCR raises the offset and amplitude terms and generally improves stability. For the same parameter settings, resistance-grounded faults provide a larger transient stability region than reactance-grounded faults, while the influence trends of the other grid parameters remain similar. This demonstrates that an inductive transition impedance has a stronger negative effect on stability than a resistive transition impedance. The proposed analytical model clarifies how fault parameters and grid strength shape the transient power-angle behavior of GFMs, and it can support fault ride-through control design and transient stability evaluation.

ACKNOWLEDGMENT

The project was supported by Research on Accuracy Evaluation Technology for Electromagnetic Transient Models of Low-Frequency Renewable Energy Generating Units, State Grid Jibei Electric Power Research Institute, 2025–2026 (SGJBDK00ZDJS2500057).

REFERENCES

[1] W. R. Kenyon, M. Bossart, M. Marković, et al., "Stability and control of power systems with high penetrations of inverter-based resources: An accessible review of current knowledge and open questions," Sol. Energy, vol. 210, pp. 149–168, 2020.

[2] S. Bahram, J. Nicklas, E. Robert, et al., "An overview of stability challenges for power-electronic-dominated power systems: The grid-forming approach," IET Gener. Transm. Distrib., vol. 17, no. 2, pp. 284–306, 2022.

[3] X. Wang, M. G. Taul, H. Wu, et al., "Grid-synchronization stability of converter-based resources: An overview," IEEE Open J. Ind. Appl., vol. 1, pp. 115–134, 2020.

[4] X. Yan, S. Y. A. Mohamed, D. Li, et al., "Parallel operation of virtual synchronous generators and synchronous generators in a microgrid," J. Eng., pp. 2635–2642, 2019.

[5] R. Rosso, X. Wang, M. Liserre, et al., "Grid-forming converters: Control approaches, grid-synchronization, and future trends: A review," IEEE Open J. Ind. Appl., vol. 2, pp. 93–109, 2021.

[6] R. Rosso, S. Engelken, and M. Liserre, "On the implementation of an FRT strategy for grid-forming converters under symmetrical and asymmetrical grid faults," IEEE Trans. Ind. Appl., vol. 57, no. 5, pp. 4385–4397, 2021.

[7] Y. Zhang, C. Zhang, R. Yang, et al., "Current-constrained power-angle characterization method for transient stability analysis of grid-forming voltage source converters," IEEE Trans. Energy Convers., vol. 38, no. 2, pp. 1338–1349, 2023.

[8] H. Wu and X. Wang, "Design-oriented transient stability analysis of grid-connected converters with power synchronization control," IEEE Trans. Ind. Electron., vol. 66, no. 8, pp. 6473–6482, 2019.

[9] Z. Shuai, C. Shen, X. Liu, et al., "Transient angle stability of virtual synchronous generators using Lyapunov's direct method," IEEE Trans. Smart Grid, vol. 10, no. 4, pp. 4648–4661, 2019.

[10] D. Pan, X. Wang, F. Liu, et al., "Transient stability of voltage-source converters with grid-forming control: A design-oriented study," IEEE J. Emerg. Sel. Top. Power Electron., vol. 8, no. 2, pp. 1019–1033, 2020.

[11] M. Chen, D. Zhou, and F. Blaabjerg, "Enhanced transient angle stability control of grid-forming converter based on virtual synchronous generator," IEEE Trans. Ind. Electron., vol. 69, no. 9, pp. 9133–9144, 2022.

[12] X. Xiong, C. Wu, B. Hu, et al., "Transient damping method for improving the synchronization stability of virtual synchronous generators," IEEE Trans. Power Electron., vol. 36, no. 7, pp. 7820–7831, 2021.

[13] X. Xiong, C. Wu, P. Cheng, et al., "An optimal damping design of virtual synchronous generators for transient stability enhancement," IEEE Trans. Power Electron., vol. 36, no. 10, pp. 11026–11030, 2021.

[14] S. Chen, Y. Sun, X. Hou, et al., "Quantitative parameters design of VSG oriented to transient synchronization stability," IEEE Trans. Power Syst., vol. 38, no. 5, pp. 4978–4981, 2023.

[15] H. Wu and X. Wang, "A mode-adaptive power-angle control method for transient stability enhancement of virtual synchronous generators," IEEE J. Emerg. Sel. Top. Power Electron., vol. 8, no. 2, pp. 1034–1049, 2020.

[16] J. Wang, S. Ganguly, and B. Kroposki, "Experimental evaluation of impact of short-circuit ratio and X/R ratio on stability of grid-forming and grid-following inverters," in Proc. IEEE Power & Energy Society General Meeting, Austin, TX, USA, 2025, pp. 1–5.

[17] P. Wang, et al., "Power self-synchronization control of grid-forming voltage-source converters against a wide range of short-circuit ratio," IEEE Trans. Power Electron., vol. 38, no. 12, pp. 15419–15432, 2023.

[18] A. J. G. Abrantes-Ferreira, A. C. Oliveira, A. M. N. Lima, et al., "A transient stability enhancement method for grid-forming converters enabling operation across the four-quadrant range of power angle," IEEE J. Emerg. Sel. Top. Power Electron., vol. 13, no. 5, pp. 6263–6280, 2025.

[19] X. Gao, D. Zhou, A. Anvari-Moghaddam, et al., "Analysis of X/R ratio effect on stability of grid-following and grid-forming converters," in Proc. IEEE Int. Conf. Compatibility, Power Electronics and Power Engineering, Tallinn, Estonia, 2023, pp. 1–6.